

Straintronics-based magnetic tunneling junction: Dynamic and static behavior analysis and material investigation

Mahmood Barangi and Pinaki Mazumder

Citation: *Appl. Phys. Lett.* **104**, 162403 (2014); doi: 10.1063/1.4873128

View online: <http://dx.doi.org/10.1063/1.4873128>

View Table of Contents: <http://aip.scitation.org/toc/apl/104/16>

Published by the [American Institute of Physics](#)

Straintronics-based magnetic tunneling junction: Dynamic and static behavior analysis and material investigation

Mahmood Barangi^{a)} and Pinaki Mazumder

Department of Electrical Engineering and Computer Science, University of Michigan, Ann Arbor, Michigan 48109-2121, USA

(Received 23 February 2014; accepted 13 April 2014; published online 22 April 2014)

We theoretically study the dynamic and static effects of mechanical stress on a straintronics device that includes a piezoelectric film combined with a magnetic tunneling junction. The inverse magnetostriction effect is studied in detail by realizing the varying magnetic susceptibility of the nanomagnet under stress. A dynamic model is developed based on the Landau-Lifshitz-Gilbert (LLG) equation, which provides a platform to simulate the magnetization vector's behavior, critical flipping voltage, and delay properties. Furthermore, by converting the LLG equation into a 2nd order damping differential equation, we develop a proximate approach. This approach predicts the dynamic behavior of the magnetization vector and its dependency on material properties and applied voltage across the device without using sophisticated numerical calculations of the LLG model. Different dynamic and static material properties are observed by simulating five common magnetostrictive materials, including a newly discovered alloy, Galfenol. © 2014 AIP Publishing LLC. [<http://dx.doi.org/10.1063/1.4873128>]

As integrated circuits (ICs) continue to progress, smaller device sizes lead to more leakage power and higher energy density.¹ The high leakage issue is mainly because charge-based logic and memories are usually volatile and need to be continuously connected to supply voltage, even when the system is computationally inactive. In order to alleviate the high leakage issue, magnetic tunneling junction (MTJ)-based memories are good representatives of non-volatility. These types of memories perform read and write at high speeds. Furthermore, the theoretical switching energy of magnetic logic is much lower than that of charge-based logic² ($E_{mag} = E_{CMOS}/N$, with N being the number of charge carriers in complementary metal-oxide-semiconductor (CMOS) logic). Field induced magnetic switching³ (FIMS) and spin transfer torque⁴ (STT) switching are the most common approaches used to write into magnetic logics. These conventional approaches, however, are based on the flow of high static currents, which makes magnetic logic energy inefficient. This leaves the window wide open for a non-current-based approach to remove the low energy efficiency obstacle of the conventional MTJ-based designs.

Applying stress and using the inverse magnetostriction effect (Villari effect) is an alternative to STT and FIMS to switch the magnetization state of a MTJ. It has been reported and analyzed that magnetic susceptibility and, therefore, magnetic permeability of rocks change when the rock samples are uniaxially compressed across an axis.⁵ This leads to a change in the intrinsic magnetic anisotropy energy of the magnet in different directions and, therefore, can create an energy minimum for the magnetization vector. This is the basis of the Villari effect.

For decades, a combination of magnetostriction/Villari effect and piezoelectricity has been used in order to generate an electric voltage when the device is subject to an external

magnetic field or vice versa.^{6–8} This is done by interfacing a magnetostrictive layer and a piezoelectric layer (PZT) so as to transfer mechanical stress between the layers. Most of the works in this area focus on the use of the magneto-electric effect by sensing a voltage change across PZT as a result of the magnetization changes in the magnetostrictive layer as shown in Fig. 1(a). This can be widely used in sensor design. Recently, the principle of using an applied voltage across PZT to assist with the flipping of the magnetization vector in a magnetostrictive layer has been the subject of academic research.^{9,10} This is the basis of the straintronics principle, which is used to avoid high static currents in FIMS and STT while switching the MTJ's state. This establishes a bridge to get closer to the theoretical energy limit of magnetic logic discussed earlier.

Although straintronics has attracted a lot of research attention recently, most of the focus has been on the proof of concept and single magnet flipping. In order to be able to exploit straintronics in ubiquitous ICs, PZT needs to be incorporated with the MTJ. In this Letter, we thoroughly explore the dynamic and static behavior of the PZT-MTJ device in order to establish a unique model that can be used to interface the straintronics device (STR) with CMOS circuitry in ICs. Different magnetostrictive materials with extremes in terms of magnetostriction expansion at saturation, Gilbert damping factor, and saturation magnetization are analyzed.

We will first investigate the effect of stress on different magnetostrictive materials by updating the susceptibility model by Nagata⁴ for our ferromagnetic materials. Then we will develop a dynamic model based on the Landau-Lifshitz-Gilbert (LLG) equation. Five different materials will be simulated using these models for their static and dynamic behavior under mechanical stress. We will conclude the Letter by developing a dynamic approximation for the magnetization behavior of the device under an applied stress. This approximation model can be used to closely predict the

^{a)}Email: barangi@umich.edu

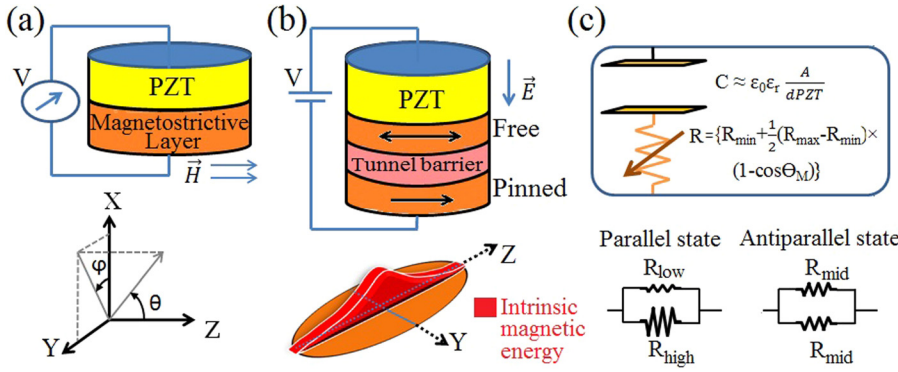


FIG. 1. (a) Conventional PZT/magnetostrictive layer interface. The magnetic field causes deformation in bottom layer, which is transferred to PZT results in electrical voltage in multimeter, (b) PZT-MTJ interface in STR. The device has the lowest magnetic energy along the major axis. (c) The equivalent electrical model of STR; the PZT and MTJ are modelled as a capacitance and a variable magnetoresistance, respectively.

dynamic behavior of the magnetization vector without requiring a sophisticated numerical simulation platform.

The architecture of our proposed straintronics-based MTJ is shown in Fig. 1(b). The device shape is a cylindrical ellipse. PZT is made with Lead-Zirconate-Titanate and is four times thicker than the free magnet with a large plane interface to assure complete transfer of the stress. In the absence of any stress, free layer's magnetization vector settles at parallel (low resistance) or antiparallel (high resistance) orientation along the z -axis (major axis) due to the magnetic energy minimum in this direction. The equivalent resistance-capacitance (RC) model of the device is given in Fig. 1(c). An applied voltage across the device creates an electric field. This field, E , leads to a strain, S , due to the generalized Hooke's law. This strain is transferred to the free layer through the PZT-MTJ interface. When stress is applied across the magnet, magnetic susceptibility, χ_v , which establishes a connection between the magnetization, M , and the applied magnetic field, H , as $M = \chi_v H$, can increase or decrease due to positive or negative magnetostriction, respectively. Depending on the polarity of the applied voltage, the y -component of χ_v can decrease, which lowers the intrinsic magnetic energy along the y -axis (minor axis). This assures alignment of the magnetization vector along the minor axis at high stress values.

As stress is applied across the magnet, the parallel component of the magnetic susceptibility, $\chi_{v\parallel}$, decreases, while the perpendicular component, $\chi_{v\perp}$, starts to increase. The parallel and perpendicular components of the magnetic susceptibility include⁵

$$\chi^{\parallel}(\sigma) = \frac{\chi_0}{1 + \beta\sigma}, \quad (1)$$

$$\chi^{\perp}(\sigma) = \frac{\chi_0}{1 + \sqrt{k^2 + \frac{1}{4}\beta^2\sigma^2 - (k + \frac{1}{2}\beta\sigma)}}, \quad (2)$$

where σ is the applied stress and the parameters β and k depend on material properties and are given as follows:

$$\beta = \frac{3\lambda_s}{\mu_0 N_{sh} M_S^2 + \frac{4K_u}{3\pi}}, \quad (3)$$

$$k = \frac{\frac{4K_u}{2\pi}}{\mu_0 N_{sh} M_S^2 + \frac{4K_u}{3\pi}}, \quad (4)$$

where λ_s is the magnetostriction saturation at expansion; N_{sh} is the shape anisotropy coefficient; M_S is the saturation magnetization; and K_u is the uniaxial anisotropy coefficient. The values of β and k for our magnetostrictive materials range between 10^{-9} – 10^{-7} and 10^{-4} – 10^{-2} , respectively. According to (1) and (2), parallel susceptibility decreases and approaches zero for very high values of stress. Perpendicular susceptibility, however, increases and reaches a final value for high values of stress. Since the value of k is very small, at high values of stress, Taylor series approximations can be applied to obtain: $\chi^{\perp}(\sigma)|_{\sigma \rightarrow \infty} = 1 + k$.

Five magnetostrictive materials are analyzed in this Letter: Nickel with a low M_S ; Cobalt with a low Gilbert damping factor; Metglas with a high Gilbert damping factor and a low λ_s ; Terfenol-D with a high λ_s ; and Galfenol with a high M_S and a relatively high λ_s . The values of these parameters for different materials are listed in Table I. Given these parameters and by using (1) and (2), we can obtain the directional susceptibilities of different magnets when a stress (σ) is applied across the device. This is plotted in Fig. 2(a), where the values of susceptibilities are normalized to χ_0 . Terfenol-D shows the fastest drop in the value of $\chi_{v\parallel}$ due to its high magnetostriction expansion at saturation. Metglas, on the other hand, shows a slow reduction of $\chi_{v\parallel}$ since it has a very small magnetostriction expansion at saturation. The values of $\chi_{v\perp}$ are redrawn in Fig. 2(b) to show the final value of perpendicular susceptibility for different materials. Nickel, Terfenol-D, and Galfenol reach the final value faster since the value of k is much smaller for these materials. The

TABLE I. Material properties of different magnetostrictive materials simulated in this paper.

Property	Description	Terfenol-D	Nickel	Galfenol	Cobalt	Metglas
M_S (kA/m)	Saturation magnetization	800	484	1300	800	800
K_u (J/m ³)	Uniaxial anisotropy coefficient	60	5	400	450	230
$ \lambda_s $ (ppm)	Saturation magnetization at expansion	600	20	200	20	12
α	Gilbert damping factor	0.1	0.045	0.04	0.01	0.2

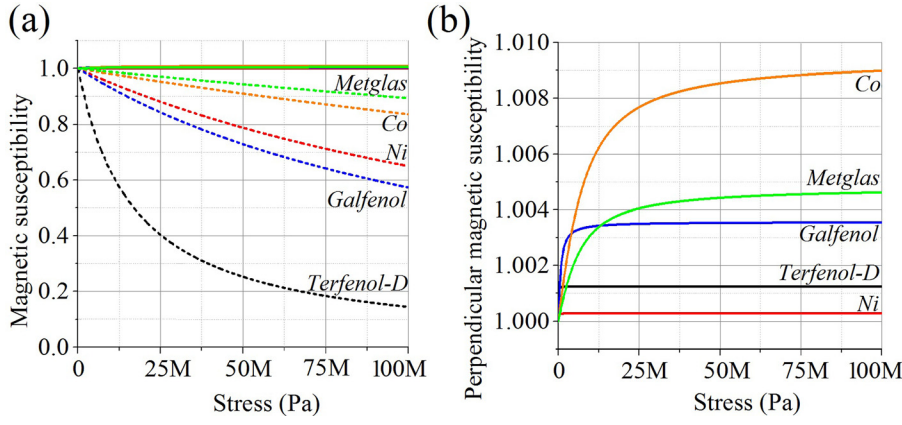


FIG. 2. (a) Directional magnetic susceptibility vs. applied stress for different magnetostrictive materials. Values are normalized to χ_0 . (b) Perpendicular component of magnetic susceptibility shows different saturation levels for different materials.

values of directional susceptibilities for different materials at $\sigma = 100$ MPa are given in Table II.

The intrinsic magnetic energy of the free magnet is mainly due to the shape anisotropy energy, E_{sh} , and the uniaxial anisotropy energy, E_u . In the absence of stress, magnetization tends to align itself along the major axis, since it is the intrinsic magnetic energy minimum as demonstrated in Fig. 1(b). As we apply stress on the free layer, $\chi_{v\parallel}$ starts to decrease, while $\chi_{v\perp}$ increases slightly. This leads to an increased shape anisotropy energy along the major axis and decreased shape anisotropy energy along the minor axis. This change continues until the total magnetic energy barrier between the major axis and the minor axis vanishes. It can be shown¹¹ that the energy barrier vanishes when

$$\left\{ \frac{1}{2} \mu_0 M_S^2 \left(N_z \frac{\chi_{\perp}(\sigma)}{\chi_0} - N_y \frac{\chi_{\parallel}(\sigma)}{\chi_0} \right) \right\} \approx K_u, \quad (5)$$

where N_y and N_z are the directional shape anisotropy coefficients. Using (2), (3), and (6), the critical stress, σ_c , that is required for flipping the magnetization state can be numerically obtained. The values of σ_c for different materials are listed in Table II. As expected, Terfenol-D shows the lowest critical flipping stress, while Metglas has the highest flipping stress.

The dynamic behavior of the free layer's magnetization vector, \vec{M} , can be accurately modeled using the LLG equation in Gilbert form¹²

$$\frac{d\vec{M}}{dt} = -\frac{\gamma_0}{(1+\alpha^2)} (\vec{M} \times \vec{H}) - \frac{\gamma_0}{M_S \times \left(\alpha + \frac{1}{\alpha} \right)} \vec{M} \times (\vec{M} \times \vec{H}), \quad (6)$$

TABLE II. Magnetic susceptibility values at 100 MPa stress and critical flipping stress based on variable susceptibility model and LLG model.

Simulated property	Terfenol-D	Nickel	Galfenol	Cobalt	Metglas
$\left(\frac{\chi_{\perp}}{\chi_0} \right)_{\sigma=100\text{MPa}}$	1.0013	1.0003	1.0036	1.009	1.0046
$\left(\frac{\chi_{\parallel}}{\chi_0} \right)_{\sigma=100\text{MPa}}$	0.145	0.650	0.573	0.836	0.895
σ_c from susceptibility model (Pa)	1.33M	14.86M	11.79M	52.33M	77.08M
σ_c from LLG model (Pa)	1.38M	14.64M	11.88M	54.45M	78.46M
V_c (V)	12 m	16 m	48 m	65 m	165 m

where γ_0 is the gyromagnetic ratio, α is the Gilbert damping factor, and \vec{H} is the effective net magnetic field acting upon the magnetization vector. The effective net magnetic field is mainly due to the shape anisotropy, uniaxial anisotropy, and stress anisotropy. Equation (6) is used to obtain the instantaneous magnetization angles (θ and φ in Fig. 1(a)) at any given voltage across the STR. With a high-enough voltage, critical stress can be achieved and the magnetization vector flips towards the minor axis. The voltage associated with this stress value is called critical voltage. By equating the intrinsic energies and the stress energy, the critical voltage can be obtained and is given as

$$V_c = \frac{\left(\frac{\mu_0}{2} M_S^2 (N_y - N_z) + K_u \right) t_{PZT}}{\frac{3}{2} \lambda_s Y d_{31}}, \quad (7)$$

where t_{PZT} is the thickness of the PZT, Y is the Young modulus of the free magnet, and d_{31} is the piezoelectric effect coefficient. The values of critical voltages for different materials with the same cylindrical ellipse geometry of Fig. 1(b) (where, $a = 205$ nm, $b = 195$ nm, and $t = 10$ nm) are tabulated in Table II.

Equation (6) can be used to simulate the dynamic behavior of the STR. A voltage higher than V_c will make the magnetization vector align itself towards the minor axis. In order to study the straintronics principle better, we simulated the effect of the magnetostriction expansion at saturation on the alignment delay. The results are shown in Fig. 3(a), where a 0.5 V voltage is abruptly applied across the device and the alignment delay is observed. For each plot in the graph, all of the magnetic properties of a material (except for λ_s) are kept constant and different values of λ_s are simulated. The points on the graph that are associated with the materials are starred. The graph indicates that the alignment delay decreases as λ_s increases. According to the graphs, a magnetostrictive material with magnetic properties of cobalt and λ_s of Terfenol-D (if existed) would guarantee a very fast response.

Equation (6) also predicts the dependency of the alignment delay on the amplitude of the applied voltage across the device, which is simulated and plotted in Fig. 3(b) for the five materials. Higher voltages lead to faster response, while voltages close to critical voltage lead to high delays.

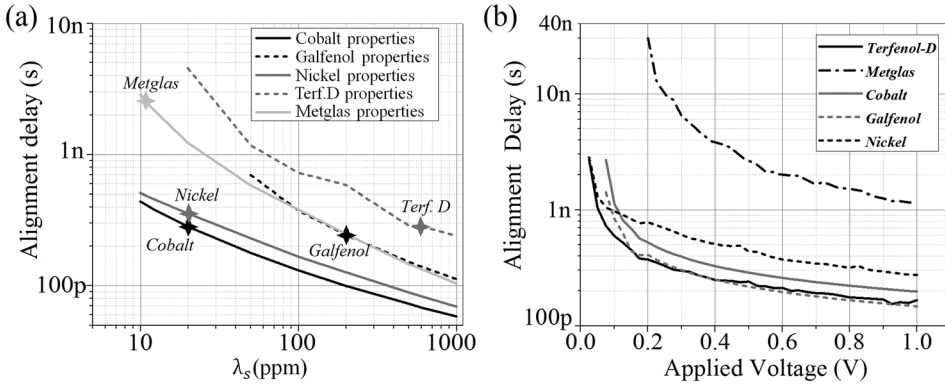


FIG. 3. (a) Alignment delay as a function of magnetostriction expansion at saturation. For each plot, the magnetic properties of a magnet are kept the same while sweeping its λ_s value. (b) Alignment delay of the materials decrease as the amplitude of the applied voltage increases.

The LLG model predicts different critical flipping voltages for different materials. The relation between critical stress and critical voltage needs to be mentioned here. While we physically apply a voltage across the straintronics device, the direct cause of the magnetization vector's flipping is the mechanical stress. Critical stress that causes flipping is proportional to Young modulus. Therefore, Terfenol-D, which exhibits a critical voltage close to nickel in Table II, has a much lower critical stress compared to nickel. This is due to lower Young modulus of Terfenol-D. The values of the critical stress from LLG model are tabulated in Table II. A comparison between these values and the values of the critical stress from the susceptibility model confirms the legitimacy of (5).

Although LLG equation provides an accurate model for magnetization vector flipping, it needs to be solved numerically. A simplified dynamic model that predicts the damping behavior of the magnetization vector without requiring sophisticated numerical computations can be developed by simplifying (6) using Taylor series approximations. The damping behavior of the magnetization vector when aligning towards the minor axis can be estimated

using the second degree control equation for damping ($d^2\theta/dt^2 + 2\zeta\omega_0 d\theta/dt + \omega_0^2\theta = 0$, ζ : general damping factor, ω_0 : natural frequency). By simplifying the LLG-model and using the Taylor series approximations,¹¹ ζ and ω_0 can be obtained as

$$\zeta = \frac{\alpha(M_1 + M_2)}{\sqrt{4(1 + \alpha^2)M_1M_2 - \alpha^2(M_1 + M_2)^2}}, \quad (8)$$

$$\omega_0 = \frac{\sqrt{4(1 + \alpha^2)M_1M_2 - \alpha^2(M_1 + M_2)^2}}{2}, \quad (9)$$

$$\theta(t) = \frac{\pi}{2} - \frac{\pi}{2} e^{-\zeta\omega_0 t} \cos(\omega_d t), \quad \omega_d = \omega_0 \sqrt{1 - \zeta^2}, \quad (10)$$

where M_1 and M_2 are coefficients that depend on material properties and the applied voltage across the device, and ω_d is the oscillation frequency of the magnetization vector while damping to the minor axis. This approximate model can be used to analyze the dynamic behavior of the magnetization vector for different materials and for different voltages that is applied across the device.

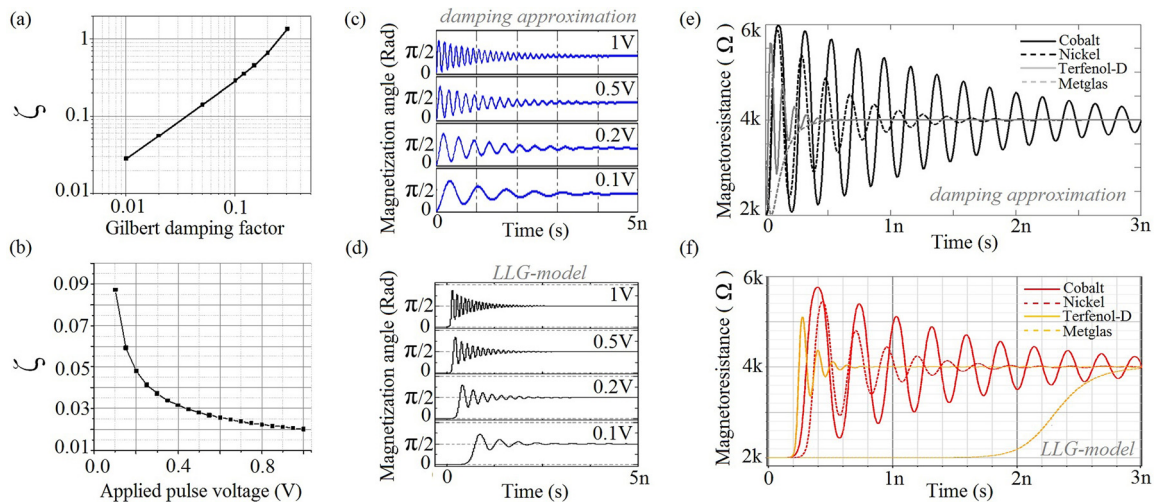


FIG. 4. (a) Dependency of general damping factor on Gilbert damping factor under 0.5 V applied voltage and using cobalt magnetic properties. (b) and (c) General damping factor of cobalt in (8) is a function of applied voltage. A higher voltage predicts a lower ζ and therefore more oscillatory behaviour is observed when damping to minor axis, (d) LLG model predicts the same dynamic behaviour while damping, (e) and (f) magnetoresistance change in MTJ when 0.5 V pulse is applied across STR and magnetization switches to minor axis. Equation (10) and LLG model predict almost the same dynamic responses, which confirm the accuracy of dynamic approximation approach.

Equation (8) predicts that the dynamic damping of the magnetization vector is a function of the Gilbert damping factor and the voltage applied across the device. This is demonstrated in Figs. 4(a) and 4(b). A higher Gilbert damping factor leads to a higher general damping factor. Fig. 4(b) predicts that ζ reduces for higher values of applied voltage. Therefore, more oscillatory behavior is expected for higher voltage amplitudes across the device, which is demonstrated by dynamic waveforms in Fig. 4(c). In order to emphasize the accuracy of the damping approximation in (10), we plotted the results of the LLG model in Fig. 4(d). The results show the same oscillatory behavior between (10) and the LLG model with some differences in their initial delay. This initial delay in the LLG model is because this model takes the initial conditions of the magnetization vector when a pulse is applied into account.

The expected dynamic response of different materials based on (10) and the LLG model are demonstrated in Figs. 4(e) and 4(f), respectively, where we applied a 0.5 V pulse across the devices and observed their magnetoresistance change. The dynamic response of different materials, excluding the initial delay of the LLG model due to initial conditions, is almost the same between the LLG model and (10). As expected from (8), for Metglas, the dynamic approximation predicts no oscillatory behavior since $\zeta_{Metglas} > 1$, while Terfenol-D has slight oscillations since $\zeta_{Terfenol-D} \approx 0.15$.

The dynamic approximation, along with the LLG equation and the variable-susceptibility model, creates a comprehensive platform to analyze and simulate the magnetization behavior of the straintronics-based MTJ. Ultra-low energy switching of the STR along with its fast response to an applied voltage makes it a perfect candidate for a variety of applications. The STR can be used to build non-volatile memories that can operate at high frequencies while demonstrating high energy efficiencies. This can deliver the promise of the ideal memories, something that circuit designers have been striving to achieve for decades. Galfenol and

Cobalt can be the perfect candidates for high performance memories given their fast response and their moderate noise margin. Metglas can be a good candidate for magnetic hard disk drives, where a high noise margin is desired, while longer access time will not matter. The STR can also be a perfect candidate to build nonvolatile logic for energy-limited applications including biomedical devices and sensor nodes, where the system can turn on, perform calculations at a fast speed with a low energy dissipation, and turn back off without any loss of data. Terfenol-D and Nickel can be employed when switching at very low voltages is desired while low noise margins can be tolerated. Furthermore, due to low switching voltages, the STR allows magnetic memories to operate along with CMOS circuitry in deep sub-threshold regime, something that FIMS and STT magnetic memories fail to deliver due to their high switching current requirements.

This work was done partially under NSF NEB Grant No. ECCS-1124714 (PT106594-SC103006) and partially under AFOSR Grant No. FA9550-12-1-0402.

¹S. Borkar, *IEEE Micro* **19**, 23 (1999).

²S. Salahuddin and S. Datta, *Appl. Phys. Lett.* **90**, 093503 (2007).

³D. D. Tang, P. K. Wang, P. S. Speriou, S. Le, and K. K. Kung, *IEEE Trans. Magn.* **31**, 3206 (1995).

⁴J. Kim, K. Ryu, S. H. Kang, and S. Jung, *IEEE Trans. VLSI* **20**, 181 (2012).

⁵T. Nagata, *Pure Appl. Geophys.* **78**, 110 (1970).

⁶M. Avellaneda and G. Harshe, *J. Intell. Mater. Syst. Struct.* **5**, 501 (1994).

⁷K. H. Shin, M. Inoue, and K. I. Arai, *IEEE Trans. Magn.* **34**, 1324 (1998).

⁸J. Ryu, *Jpn. J. Appl. Phys., Part 1* **40**, 4948 (2001).

⁹K. Roy, *Appl. Phys. Lett.* **99**, 063108 (2011).

¹⁰J. Atulasimha, *Appl. Phys. Lett.* **97**, 173105 (2010).

¹¹See supplementary material at <http://dx.doi.org/10.1063/1.4873128> for critical stress of the magnetic susceptibility model and the dynamic approximation calculations.

¹²F. G. Sanchez, Ph.D. dissertation, Universidad Autonoma de Madrid, 2007.